Missouri University of Science and Technology
Scholars' Mine

Materials Science and Engineering Faculty Research & Creative Works

Materials Science and Engineering

01 Sep 2022

# Ultrafast Stiffening of Concentrated Thermoresponsive Mineral Suspensions

Sharu Bhagavathi Kandy

Iman Mehdipour

Narayanan Neithalath

Aditya Kumar
*Missouri University of Science and Technology*, kumarad@mst.edu

*et. al. For a complete list of authors, see https://scholarsmine.mst.edu/matsci_eng_facwork/2873*

Follow this and additional works at: https://scholarsmine.mst.edu/matsci_eng_facwork

 Part of the Materials Science and Engineering Commons

## Recommended Citation

S. Bhagavathi Kandy et al., "Ultrafast Stiffening of Concentrated Thermoresponsive Mineral Suspensions," *Materials and Design*, vol. 221, article no. 110905, Elsevier, Sep 2022.
The definitive version is available at https://doi.org/10.1016/j.matdes.2022.110905

This work is licensed under a Creative Commons Attribution 4.0 License.

This Article - Journal is brought to you for free and open access by Scholars' Mine. It has been accepted for inclusion in Materials Science and Engineering Faculty Research & Creative Works by an authorized administrator of Scholars' Mine. This work is protected by U. S. Copyright Law. Unauthorized use including reproduction for redistribution requires the permission of the copyright holder. For more information, please contact scholarsmine@mst.edu.

Materials & Design 221 (2022) 110905

Contents lists available at ScienceDirect

Materials & Design

journal homepage: www.elsevier.com/locate/matdes

# Ultrafast stiffening of concentrated thermoresponsive mineral suspensions

Sharu Bhagavathi Kandy [a,b], Iman Mehdipour [a,b], Narayanan Neithalath [c], Aditya Kumar [d], Mathieu Bauchy [b,e], Edward Garboczi [f], Samanvaya Srivastava [b,g,h,i], Torben Gaedt [j,*], Gaurav Sant [a,b,i,k,*]

[a] Laboratory for the Chemistry of Construction Materials (LC$^2$), Department of Civil and Environmental Engineering, University of California, Los Angeles, CA 90095, USA
[b] Institute for Carbon Management (ICM), University of California, Los Angeles, CA 90095, USA
[c] School of Sustainable Engineering and the Built Environment, Arizona State University, Tempe, AZ 86587, USA
[d] Department of Materials Science and Engineering, Missouri University of Science and Technology, Rolla, MO 65409, USA
[e] Laboratory for the Physics of AmoRphous and Inorganic Solids (PARISlab), Department of Civil and Environmental Engineering, University of California, Los Angeles, CA 90095, USA
[f] Applied Chemicals and Materials Division, Material Measurement Laboratory, National Institute of Standards and Technology, Boulder, CO 80305, USA
[g] Department of Chemical and Biomolecular Engineering, University of California, Los Angeles, CA 90095, USA
[h] UCLA Center for Biological Physics, University of California, Los Angeles, CA 90095, USA
[i] California Nanosystems Institute (CNSI), University of California, Los Angeles, CA 90095, USA
[j] Department of Chemistry, Technische Universität München, Lehrstuhl für Bauchemie, Lichtenbergstrasse 4, D-85747 Garching bei München, Germany
[k] Department of Materials Science and Engineering, University of California, Los Angeles, CA 90095, USA

## HIGHLIGHTS

- A facile pathway to achieve controllable, rapid stiffening in aqueous suspensions that are compatible with extrusion-based 3D printing.
- Thermoresponsive-concentrated mineral suspensions are formulated using thermally triggered epoxy-thiol condensation-polymerization reactions.
- Thermal latency, tunable induction period, and rapid stiffening are realized in concentrated mineral suspensions.
- Suspensions exhibit rapid solidification in timescales of seconds to minutes upon bulk thermal activation, achieving average stiffening rates up to 400 Pa/s.
- Offer new pathways to overcome the limitations of traditional suspension-based printing and expand the design and production space accessible for architected structural components.

## GRAPHICAL ABSTRACT

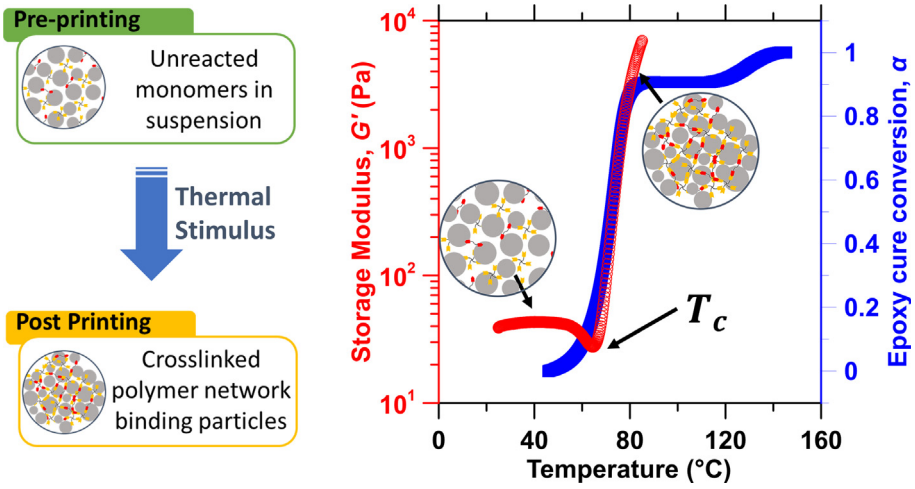


## ARTICLE INFO

*Article history:*
Received 20 November 2021
Revised 24 April 2022

## ABSTRACT

Extrusion-based 3D printing with rapidly hardening polymeric materials is capable of building almost any conceivable structure. However, concrete, one of the most widely used materials for large-scale structural components, is generally based on inorganic binder materials like Portland cement. Unlike

* Corresponding authors.
*E-mail addresses:* torben.gaedt@tum.de (T. Gaedt), gsant@ucla.edu (G. Sant).

https://doi.org/10.1016/j.matdes.2022.110905
0264-1275/© 2022 The Author(s). Published by Elsevier Ltd.
This is an open access article under the CC BY-NC-ND license (http://creativecommons.org/licenses/by-nc-nd/4.0/).

Accepted 26 June 2022
Available online 4 July 2022

*Keywords:*
Ultrafast stiffening
3D printing
Additive manufacturing
Thermoresponsive suspensions
Stimuli-responsive suspensions
Epoxy-thiol polycondensation

polymeric materials, a lack of precise control of the extent and rate of solidification of cement-based suspensions is a major issue that affects the ability to 3D-print geometrically complex structures. Here, we demonstrate a novel method for controllable-rapid solidification of concentrated mineral suspensions that contain a polymer binder system based on epoxy and thiol precursors as well as one or more mineral fillers like quartz and calcite. The thermally triggered epoxy-thiol condensation polymerization induces rapid stiffening of the hybrid suspensions ($0.30 \leq \phi \leq 0.60$), at trigger temperatures ranging between 50 °C and 90 °C achieving average stiffening rates up to 400 Pa/s. The use of nucleophilic initiators such as 1-methylimidazole provides control over the activation temperature and curing rate, thereby helping to achieve an adjustable induction period and excellent thermal latency. By using multiple techniques, we provide guidelines to create designer compositions of mineral suspensions that utilize thermal triggers to achieve thermal latency and ultrafast stiffening – prerequisite attributes for 3D-manufacturing of topologically-optimized structural components.

© 2022 The Author(s). Published by Elsevier Ltd. This is an open access article under the CC BY-NC-ND license (http://creativecommons.org/licenses/by-nc-nd/4.0/).

## 1. Introduction

With a growing demand for more complex construction components and a general trend towards prefabrication of structural components, slurry-based 3D printing is a promising additive manufacturing method capable of outperforming conventional construction practices. Slurry-based 3D printing reduces material utilization, enables higher geometrical complexity, shortens construction time, decreases labor demand, simplifies construction logistics, and lowers construction costs [1–5]. To significantly reduce material consumption in construction, a promising approach lies in topologically-optimized structures obtained via additive manufacturing processes [6,7]. However, the topologically-optimized structures are often geometrically more complex, having spatially inclined parts within the structure [8,9]. Printing of spatially inclined members in a structure usually requires an overhang (i.e., the portion of the subsequent extruding layer beyond the length of the previously printed layer), and the extent of the overhang is limited by the rate of stiffening of printing slurry. A central issue that impedes the implementation of layer-wise extrusion-based 3D printing for geometrically complex structures is the slow and difficult to control evolution of the mechanical properties (e.g., yield stress, elastic modulus, and stiffness) of slurry-based "printing inks" following their deposition [10–14]. Rheology control and the optimal stiffness evolution are essential factors that govern the printability of structures and are often used to predict printability [10–12,15–19]. The slow fluid-to-solid transition of typical inorganic mineral binders greatly restricts the palette of printable geometries, especially of structures with overhangs, limiting achievable architectures. To truly exploit the opportunities unlocked by generative design, topology optimization, and 3D printing, it is essential to develop printable compositions that can undergo rapid stiffening in a manner of seconds to minutes, thereby turning into a "semi-solid" that can bear its own weight and the subsequent few layers above it.

Layered extrusion with cementitious suspensions (i.e., concrete 3D printing) requires slow stiffness build-up before extrusion (i.e., during storage and pumping) followed by rapid stiffening after deposition. In typical cementitious suspensions, the extent and rate of solidification depend on the hydration of cement along with a minor contribution of colloidal flocculation [20]. Various approaches for hydration control have been attempted to ensure structural stability during concrete 3D printing, including a variety of mineral binder compositions (i.e., ordinary Portland cement, calcium sulfoaluminate cement, calcium aluminate cement) [21,22], use of various organic admixtures (e.g., set accelerators and retarders) [23] and set-on-demand admixtures (i.e., controlled activation of hydration shortly before material deposition) [14]. However, use of engineering cement-based printing slurry formulations to induce a controllable ultrafast stiffening or achieve precise control over the yield stress/ strength evolution to the degree required for additive manufacturing of a wide range of structures while relying exclusively on the hydration of cement remains challenging [12,23].

Active control approaches, wherein external stimuli, including mechanical, photochemical, thermal, pressure, electric, magnetic, and microwave interventions, are applied anytime during or after the deposition of the ink to control the stiffening process [24], have afforded significant acceleration and greater control over the fluid-to-solid transition during 3D-printing [25–30]. For example, controllable stiffening in polymerizable mineral suspensions has been extensively used in gel casting [31,32], ceramic stereolithography [29,30], and tape casting [33]. In such polymerizable mineral suspensions, heat or UV irradiation is used to initiate a polymerization reaction that induces gelation in the suspension. While rapid fluid-to-solid transitions have been obtained in photo-polymer based systems [29,30], these approaches are not scalable for the production of opaque, low-surface to volume ratio, and often poorly (thermal and electrical) conductive structural materials. New approaches for triggering controllable rapid solidification in cementitious suspensions are therefore necessary to enable additive manufacture of topology optimized structural components that demand rapid hardening and high early strength.

In this paper, we demonstrate a methodology and design strategy for utilizing thermal triggers to compose concentrated-mineral suspensions that achieve desirable thermal latency, have a tunable induction period, and demonstrate ultrafast stiffening – prerequisites for 3D-manufacturing of architected structural components for construction. We demonstrate mineral suspensions that exhibit an adjustable induction period at room temperature to provide workability, followed by ultrafast fluid-to-solid transitions and stiffening upon imposition of a thermal activation at trigger temperatures ranging between 50 °C and 90 °C. Such activation is achieved by exploiting the temperature dependence of 1-methylimidazole catalyzed thiol-epoxy "click reactions". The basic concept is as follows: once heated above the activation temperature, the reaction of a thiol and an epoxy group, initiated using an appropriate base (e.g., hydroxides or tertiary amines), yields $\beta$-hydroxythio-ethers [34–38]. The thiol-epoxy reaction is strongly autocatalytic and progresses rapidly once initiated due to the formation of alkoxide anions generated during the reaction that facilitate the ring-opening of the epoxides [34,36,39,40]. This reaction pathway offers a facile route to control the thermal latency and stiffening rate of mineral suspensions. Based on this approach, we achieve rapid stiffening in aqueous suspensions that are amenable to extrusion-based additive manufacturing process by: forming a thermoresponsive concentrated-aqueous suspension; applying controlled heating in the print nozzle to achieve rapid stiffening during extrusion; and exposing the structural component to post-curing for further strength gain. Taken together, the

outcomes of this work offer new pathways to overcome the limitations of traditional suspension-based printing and expand the design and production space accessible for manufacturing complex, topologically optimized structural components for construction.

## 2. Materials and methods

### 2.1. Materials

Waterborne epoxy resin EPI-REZ 7510-W 60 was obtained from Hexion Chemicals[1] (epoxy equivalent weight = 197 g $eq^{-1}$, density at 25 °C: 1100 kg $m^{-3}$). EPI-REZ 7510-W 60 is a nonionic, aqueous dispersion of bisphenol A epoxy resin particles (1 μm – 2.2 μm) comprising ~61 mass % solids. GABEPRO GPM-800, a mercaptan-terminated liquid crosslinking agent (thiol equivalent weight: 250 g –333 g $eq^{-1}$, density 1150 kg $m^{-3}$) was obtained from Gabriel Chemicals. The nucleophilic initiator 1-methylimidazole (MI) was obtained from ACROS Organics. Two different polydisperse mineral particulates were used to prepare the thermosensitive suspensions including commercially available quartz (α-$SiO_2$, MINUSIL 5, U.S. Silica, density = 2650 kg $m^{-3}$) and limestone (calcite [$CaCO_3$], OMYACARB UF - FL, Omya Inc., density = 2710 kg $m^{-3}$). All chemicals were used as received.

The particle size distributions of the particulates were measured on dilute suspensions of particles (0.002 vol%) in deionized water using static light scattering (SLS; Partica LA-960A2, Horiba). The median particle diameter ($d_{50}$) of the quartz was 1.95 μm ± 0.005 μm and for the calcite particles, $d_{50}$ = 2.01 μm ± 0.01 μm. The uncertainty represents the standard deviation based on three replicate measurements. A commercially available polycarboxylate ether-based dispersant (MasterGlenium 7500, Master Builders Construction Chemicals) was dosed at 0.5 % (ratio of dry mass of dispersant to mass of mineral particulates) to disperse the hydrophobic thiol crosslinking agent in water and improve particulate dispersion in the suspension.

### 2.2. Sample preparation

Resin mixtures with different thiol-to-epoxy mass ratios, $r$, ranging between 0.50 and 1.5 were prepared. The initiator proportion, $x$, was varied between 1 and 5 % (ratio of mass of initiator to dry mass epoxy resin). The mixtures were stirred until a homogeneous-milky dispersion was obtained and tested immediately to study the curing behavior. Thermoresponsive epoxy-thiol-mineral particulate suspensions comprising one or more mineral particulates were prepared at varying solid volume fractions ($\phi$) ranging between 0.30 and 0.60 in a multistep procedure. First, the polymeric dispersant was added to deionized water, followed by the required amount of thiol crosslinking agent, calculated as per the mixing ratio, $r$. The mixture was then stirred thoroughly using a four-blade impeller-type mixer (RW 20 Digital, IKA) at 500 rpm to disperse the thiol in water. The epoxy resin and the required proportion of the initiator were then added to the dispersion and stirred using the mixer to produce a homogeneous dispersion. Subsequently, varying amounts of mineral particulates were added to the epoxy-thiol dispersion and the mixture was stirred for 300 s using the mixer. Cuboidal "beam" geometries were prepared using the thermoresponsive suspensions for mechanical strength testing by casting in a rectangular mold followed by curing at 90 °C for 24 h.

### 2.3. Differential scanning calorimetry

A differential scanning calorimeter TA Instruments DSC25 was used to study the curing kinetics of the thermoresponsive formulations. Since the epoxy-thiol resin mixture and suspensions contain water, the water evaporation endotherm masked the exothermic peaks associated with the thermoset curing in the DSC data. Hence, DSC analyses were carried out in high pressure capsules that can withstand pressures up to 10 MPa to separate the overlapping thermal events by delaying the evaporation of water. Any effect of the build-up pressure on the curing kinetics was assumed to be marginal. Approximately 20 mg of sample was placed in the high-pressure capsule and cured using different heating rates between a low temperature of 35 °C to a high temperature of 220 °C in an inert-$N_2$ atmosphere. The exothermic heat of reaction, $\Delta h_{total}$ (i.e., the enthalpy of reaction) was calculated by integration of the calorimetric signal. The cure conversion $\alpha$ (i.e., the calorimetric degree of curing) was estimated as $\alpha = \Delta h/\Delta h_{total}$, where $\Delta h$ is the reaction heat released up to a temperature $T$. The non-isothermal cure curves at {2, 5, 10, 15, and 20} °C/min were used to analyze the curing kinetics and estimate the activation energy, $E_\alpha$, as a function of the cure conversion, $\alpha$, using the model-free integral isoconversional method [41]. Further details regarding this method are provided in Section B of the Supporting Information.

### 2.4. Rheology

Thermal latency and the stiffening response of the thermoresponsive suspensions were assessed by rheology measurements on freshly prepared suspensions using a combined motor-transducer rheometer (Discovery HR-2, TA Instruments). The rheometer was equipped with a Peltier concentric cylinder jacket for temperature control and a solvent trap to minimize water evaporation. A four-bladed vane in cup geometry was used to perform small amplitude oscillatory shear (SAOS) analyses. The suspensions were subjected to a small amplitude oscillatory temperature ramp with a steady temperature increase from 25 °C to 90 °C. The thermoresponsive solidification behavior of the suspensions was monitored by the evolution of their elastic modulus $G'$ with temperature. To ensure a uniform temperature and to minimize the thermal lag, temperature ramp measurements were performed at a ramp rate of 2 °C/min.

Before temperature ramping, all suspensions were pre-sheared at 100 $s^{-1}$ for 60 s and then relaxed for 60 s to homogenize the suspension and to eliminate shear history effects. The water content of the suspensions was assessed before and after the rheology measurements using thermogravimetric analysis (TGA: STA 6000, Perkin Elmer) and showed an average change of $\leq 2$ and $\leq 5$% by mass, respectively, for suspensions with and without incorporating thermoset resins. Thus, the impact of water evaporation was assumed to be minimal. Thermal latency was assessed using the oscillatory shear rheology at a controlled temperature of 25 °C, and the temporal evolution of $G'$ was monitored for a period of up to 2 h. The oscillatory rheology measurements were performed at a fixed angular frequency of 6.283 rad/s and the strain was fixed at 0.5 %.

### 2.5. Flexural strength

The flexural strength of the cured composites was evaluated in 3-point bending using an Instron 5564 Universal Material Testing machine equipped with a 1 kN load cell. At least six beam samples were tested for each formulation. The testing was carried out on

[1] Certain commercial equipment, software and/or materials are identified in this paper in order to adequately specify the experimental procedure. In no case does such identification imply recommendation or endorsement by the National Institute of Standards and Technology, nor does it imply that the equipment and/or materials used are necessarily the best available for the purpose.

50 mm (length) × 7 mm (width) × 4 mm (thickness) samples at a constant displacement rate of 0.5 mm/min with a span length of 20 mm until fracture. The load–displacement curves were recorded, and the flexural stress was evaluated as $\sigma_f = 3Fl/2bd^2$, where $F$ is the failure load, $l$ is the span length, $b$ is the beam width, and $d$ is the beam thickness. The span length-to-depth ratio ($l/d$) used for the flexural testing was 5 as opposed to the 13.33 prescribed in ASTM C1161. The smaller $l/d$ can produce wedging stresses (i.e., the local stresses under the loading point) that modify the stress distribution on the opposite surface (the tensile side) and cause an increase in the force required to produce a given level of thin-beam flexural stress [42]. The wedging stress may cause the test samples to appear stronger than estimated by thin-beam analysis. Therefore, a correction factor of 0.90 was applied to mitigate the overestimation of the flexural strength [43].

## 3. Results and discussion

### 3.1. Controlling thermal latency and the degree of curing of epoxy-thiol mixtures

The curing kinetics of epoxy-thiol resin mixtures without mineral particulates was assessed to optimize the thiol-to-epoxy mixing ratio $r$ and the initiator dosage $x$. Fig. 1a shows DSC thermograms for epoxy-thiol resin mixtures with different ratios $r$ (at constant initiator dosage $x = 1\%$ by mass of resin). These thermograms depict the 1-methylimidazole (MI) catalyzed epoxy-thiol curing reaction as comprising two processes: a sharp exotherm representing a fast curing reaction occurring at low temperatures and a second broader exotherm indicating slower curing taking place at higher temperatures [44,45]. The first curing exotherm corresponds to MI-catalyzed epoxy-thiol curing and the sharp peak suggests a rapid curing kinetics [44,46]. The second peak at higher temperatures corresponds to MI-catalyzed anionic homopolymerization of the excess epoxy groups in formulations with a deficit of thiol groups [44,47].

The relative contributions of the first and the second curing processes depend on the thiol-to-epoxy mixing ratios, $r$ (Fig. 1a). Table 1 lists the different curing and thermal characteristics of the epoxy-thiol mixtures with different $r$ measured at 10 °C/min. The contribution of the epoxy–thiol reaction to the overall reaction heat, $\Delta h_{Total}$ is 0.99 for $r = 1.5$. This represents a near-stoichiometric mixture achieving nearly complete epoxy cure conversion $\alpha$ after the thiol–epoxy reaction (note: the theoretical value of $r$, based on the thiol and epoxy equivalent mass values, lies in the range between 1.3 and 1.7). In all the formulations with $r$ less than the stoichiometric ratio (i.e., $r < 1.5$), unreacted epoxy groups remain after the completion of the thiol-epoxy reaction. The epoxy-thiol curing process was measured to start at nearly identical onset temperatures ($T_{onset}$) for all thiol-to-epoxy ratios $r$ studied, suggesting a reaction mechanism based on initiation by thiol/amine proton exchange [39,48].

The calorimetric cure conversion ($\alpha$) curve (Fig. 1b) depicts the separation of the two cure processes and the difference in their reaction rates (Fig. 1b). The disparity between the reaction rates of the epoxy-thiol and epoxy homopolymerization processes is ascribed to the variation in the activity of the zwitterion that is formed as a result of the nucleophilic attack of the imidazole on the epoxy ring upon initiation (see reaction 1 in Scheme 1) in the presence of thiol groups [44]. In the presence of thiol groups, a fast acid-base proton exchange between the zwitterion leads to the formation of thiolate anions (reaction 2) which open the epoxy ring via nucleophilic attack to form an alkoxide anion (reaction 3) [44]. Subsequently, a fast proton transfer takes place from a thiol group (or from the β-hydroxylimidazolium cation, which is formed in reaction 2), to yield the β-hydroxythioether. The proton transfer reaction that regenerates the initiator (reaction 5) proceeds at a significantly faster rate than the nucleophilic attack of the alkoxide anion on the epoxide ring [34]. Additionally, the transfer of a proton from thiols is three orders of magnitude faster compared to the transfer from secondary alcohols [34,49]. Thus, the concentration of alkoxide anions remains very low and the epoxy homopolymerization does not occur. However, in the absence of thiol groups in the system, the rapid acid-base proton exchange reactions cannot occur, and the slower epoxy homopolymerization becomes the dominant reaction. For further details regarding the homopolymerization reaction see Scheme 1 in the Supporting Information [36,44].

The DSC thermograms in Fig. 1a depict the activation of the epoxy-thiol condensation reaction only upon reaching a specific temperature, suggesting the slow generation of active species and an induction period that can be controlled to ensure "thermal latency". Often, base-catalyzed epoxy-thiol reactions are difficult to control as they start immediately after the components are mixed, and are strongly autocatalytic [35,50]. The thiol-epoxy reaction is strongly autocatalytic due to the formation of hydroxyl-group-containing species (i.e., the $\beta$-hydroxythioether) generated during the reaction, and which can, in turn, participate in proton exchange reactions that facilitate the ring-opening of the epoxides [34,36,39]. In base-catalyzed epoxy-thiol reactions, a higher rate of production of initial thiolate anions and the concomitant increase in the formation of $\beta$-hydroxythioether lead to a poor thermal latency and short induction period. In contrast, nucleophilic initiators with low basicity, such as MI [44] and benzyldimethylamine [34] induce a slow initiation process and a subsequent strong auto acceleration up to the completion of curing at relatively lower temperatures. Imidazoles, in particular MI, also initiate anionic epoxy homopolymerization [47]. Herein, the nucleophilic initiator MI was found to initiate the epoxy-thiol curing reaction slowly, providing control over the curing process and a longer induction period [34,44].

The activation energy,$E_\alpha$, for the epoxy-thiol mixture decreased with an increase in epoxy-thiol cure conversion (see Section C and Figure S1 in the Supporting Information). The higher initial $E_\alpha$ reflects the difficult and slow initiation leading to a longer induction period and a decrease in $E_\alpha$ with increasing cure conversion reflect the autocatalytic nature of the polymerization reaction [39]. Further, a higher dosage ($x$) of the initiator resulted in a lower $T_{onset}$ and improved cure rates (Fig. 1c); in the absence of the initiator, $T_{onset}$ was the highest and the high-temperature epoxy homopolymerization did not occur over the studied temperature range (Fig. 1c).

Thus, the onset and rate of stiffening as well as the thermomechanical properties of the material can be tailored by controlling the extent of the epoxy-thiol condensation and epoxy homopolymerization by tuning the thiol-epoxy mixing ratio ($r$) in the formulation (Fig. 1a and 1b) and initiator dosage ($x$) [44]. The use of excess epoxy groups in epoxy-thiol formulations yields substantial improvements of the thermal and mechanical properties emerging from the tighter network structure resulting from the epoxy homopolymer, yielding a higher glass transition temperature (see Table 1) [44,46,49]. In these compositions, the stiffening onset temperature, the extent of stiffening, and the stiffening rate are all primarily governed by the extent of epoxy-thiol polycondensation reaction, while the final mechanical strength of the completely cured formulations is controlled by the extent of the epoxy homopolymerization reactions. Hence, it is possible to design mixture compositions that can produce: 1) targeted epoxy-cure conversion and gelation after the first curing stage (i.e., for the rapid, low-temperature epoxy-thiol curing reaction), and 2) targeted

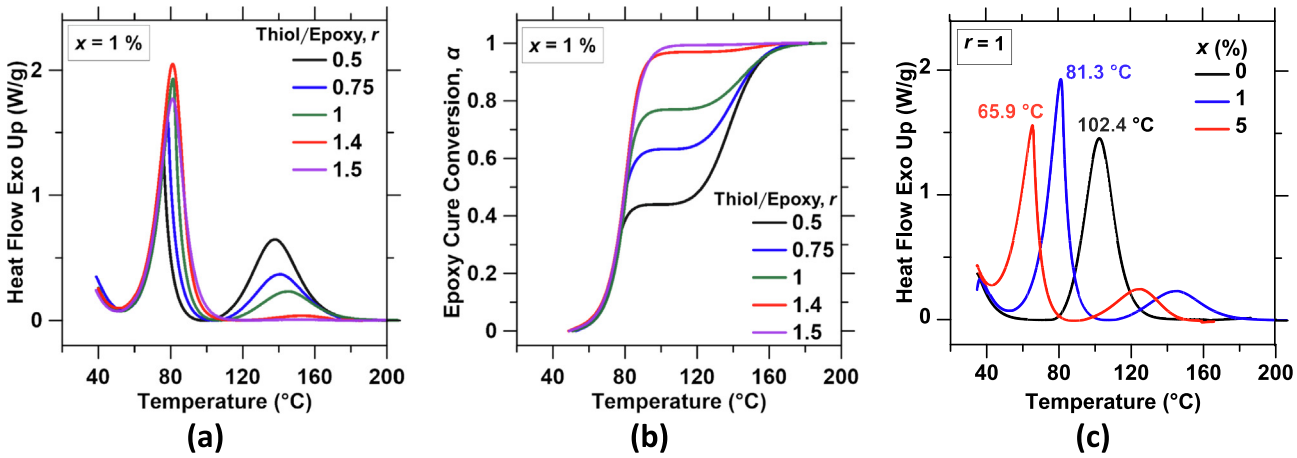


**Fig. 1.** **(a)** DSC thermograms and **(b)** calorimetric epoxy cure conversion ($\alpha$) curves illustrating the curing of epoxy-thiol resin mixture formulations with different thiol-to-epoxy mixing ratios, $r$ and fixed initiator dosage $x = 1$ % by mass of resin; **(c)** DSC thermograms of epoxy-thiol mixture formulations with different $x$ and a fixed $r = 1$. All the nonisothermal DSC data presented above were collected at a temperature ramp of 10 °C $min^{-1}$

**Table 1**
Thermal analyses of epoxy-thiol resin mixture formulations with different thiol-to-epoxy mass ratios ($r$) and fixed initiator dosage ($x = 1$ % by mass of resin) collected at a temperature ramp of 10 °C/min. Here, the epoxy-thiol curing onset temperature ($T_{onset}$), maximum peak temperature ($T_{peak}$), total heat of reaction ($\Delta h_{total}$), epoxy thiol contribution (i.e., $\Delta h_{peak1}/\Delta h_{total}$) were estimated using freshly prepared mixtures. The glass transition temperature ($T_g$) and the temperature of 10 % mass loss ($T_{10\%}$) were estimated from samples that were cured at 90 °C for 24 h.

| $r$(-) | $T_{onset}$(°C) (Peak 1) | $T_{peak}$(°C) (Peak 1) | $\Delta h_{total}$(J/g) (Peak 1 + Peak 2) | Epoxy/thiol contribution | $T_g$(°C) | $T_{10\%}$(°C) |
|---|---|---|---|---|---|---|
| 0.50 | 65.8 ± 0.1 | 75.7 ± 0.1 | 205.9 ± 2.0 | 0.41 | 56.9 ± 0.2 | 336.8 ± 3.7 |
| 0.75 | 68.1 ± 0.4 | 79.2 ± 0.5 | 196.6 ± 1.4 | 0.60 | 38.2 ± 0.4 | 331.8 ± 1.6 |
| 1.00 | 67.1 ± 0.3 | 80.4 ± 0.9 | 198.5 ± 4.6 | 0.77 | 26.3 ± 0.5 | 328.5 ± 0.6 |
| 1.40 | 67.7 ± 1.5 | 82.5 ± 1.9 | 197.5 ± 6.4 | 0.97 | 13.9 ± 1.2 | 320.7 ± 1.2 |
| 1.50 | 68.9 ± 1.4 | 84.3 ± 1.0 | 197.1 ± 2.3 | 0.99 | 14.1 ± 0.9 | 317.8 ± 1.6 |

mechanical strength upon completion of the epoxy homopolymerization.

### 3.2. *Thermomechanical behavior of mineral suspensions*

The thermoresponsive stiffening of the epoxy-thiol formulations was harnessed to induce thermally-triggered stiffening in mineral suspensions. Fig. 2a shows the evolution of the storage modulus $G'$ of concentrated suspensions of quartz, calcite, and a 40/60 mixture of quartz and calcite, with temperature. In all cases, $G'$ remained essentially unchanged below a critical temperature (i.e., stiffening onset temperature, $T_c$, estimated as the temperature at which $dG'/dt \geq 10$ Pa/s from the baseline) and an abrupt increase in $G'$ was observed when heated beyond $T_c$(see Fig. 2b). These thermostiffening responses are in stark contrast to the thermal response of suspensions without the thermoset resin that do not exhibit any appreciable increment in the value of $G'$ with temperature (see *inset* of Fig. 2a). Similar trends were observed in the dynamic loss modulus ($G''$) and the complex viscosity ($|\eta^*|$) across all suspensions, and the material response remained predominantly elastic (i.e., $G' > G''$). The increase in dynamic moduli and viscosity beyond $T_c$ is a direct result of the epoxy curing and polymer network build-up within the suspension matrix. As curing proceeds, the number of crosslinks in the polymer network and the gel fraction increase, forming a rigid 3D network around the mineral particles [51]. The crosslinked polymer networks increasingly resist the deformation and relaxation of the particle aggregates network, thereby restricting shear deformation and inducing a fluid-like to solid-like transition in the suspensions.

Interestingly, suspensions of different mineral particulates exhibited significant differences in their thermostiffening response (Fig. 2a and 2b). The thermal latency, the induction period, $T_c$, the fluid-to-solid transition temperature window and the stiffening rate all depended on the type of mineral particulates and the solid loading ($\phi$) in the suspensions (Fig. 2b). These variations can be attributed to, but not limited to, the differences in $\phi$, the dispersion state of mineral particles, particle size, particle shape, resin-mineral interactions, and the pH of the suspending medium, which in turn can influence the gelation kinetics [52–56]. Notably, resin incorporation into the mineral suspensions also resulted in a substantial increase in the low temperature $G'$ in calcite and quartz-calcite binary mixture-based suspensions. This could be ascribed to the enhanced aggregation of calcite particles around a pH of 8.2, which is close to its isoelectric point (IEP) in the pH range of 8–9.5 [57]. Nevertheless, it is evident that the epoxy-thiol resin mixture formulations can be adjusted to produce rapid, low temperature curing reactions irrespective of the mineral particles. A one-to-one correspondence between the progress in curing and stiffening is evident in Fig. 2c. A comparison of the evolution of $G'$ and the cure conversion $\alpha$ at the same heating rate (2 °C/min) for quartz suspensions ($\phi = 0.30$) demonstrates that the sharp increase in modulus takes place only after achieving a threshold epoxy cure conversion. Here, the critical Temperature $T_c \sim 70^{\circ}$C estimated from the $G'$ evolution corresponds to an epoxy cure conversion of $\alpha = 0.40$. Theoretically, gelation should occur at a certain $\alpha$ that depends primarily on the functionality of the epoxy and the thiol curing agent [58]. But, in addition to the resin and crosslinking agent functionality, solid content, particle size, particle shape, suspending medium, and use of surface treatments all affect $\alpha$ [52,59].

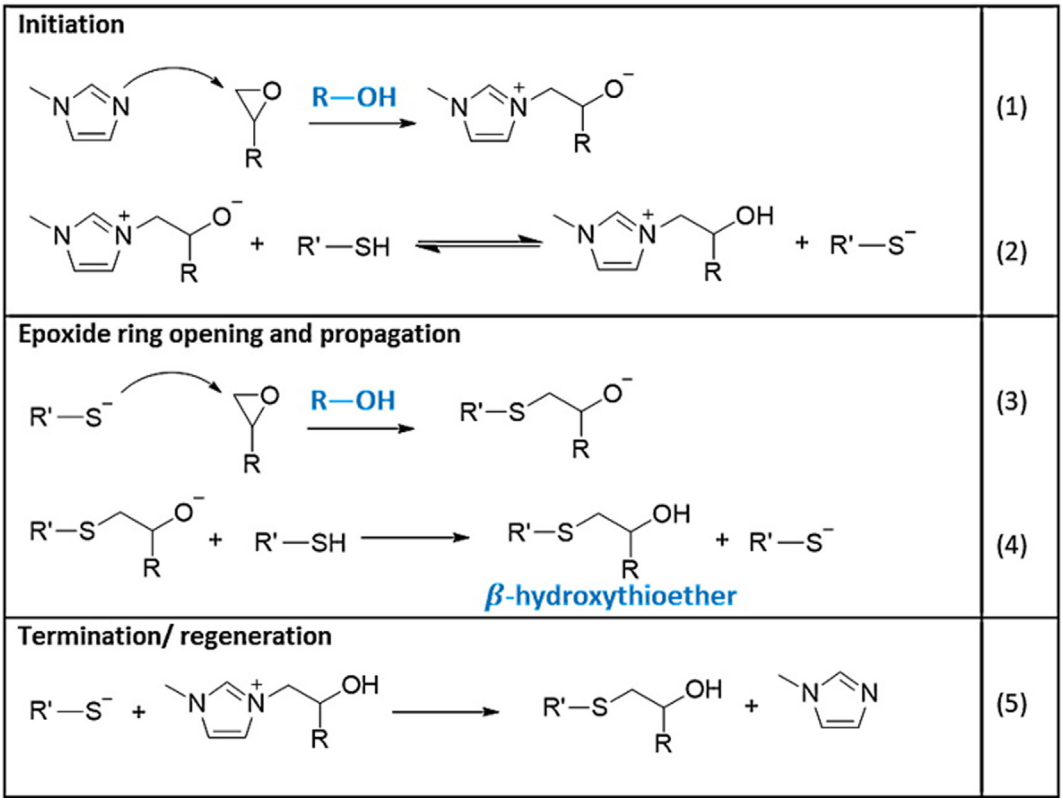


**Scheme 1.** Reaction scheme of the thiol–epoxy polycondensation catalyzed using MI (adapted from [36,44]). (1) nucleophilic attack of the imidazole on the epoxy ring resulting in the formation of the zwitterion; (2) acid-base proton exchange between the zwitterion and thiol leading to the formation of thiolate anion and β-hydroxylimidazolium cation; (3) Epoxide ring opening by thiolate anions via nucleophilic attack forming an alkoxide anion; (4) proton transfer from a thiol group (or from the β-hydroxylimidazolium cation) to alkoxide anion produce a β-hydroxythioether; (5) proton transfer reaction that regenerates MI. Here, the β-hydroxythioether (denoted as R-OH) is responsible for the autocatalytic effect.

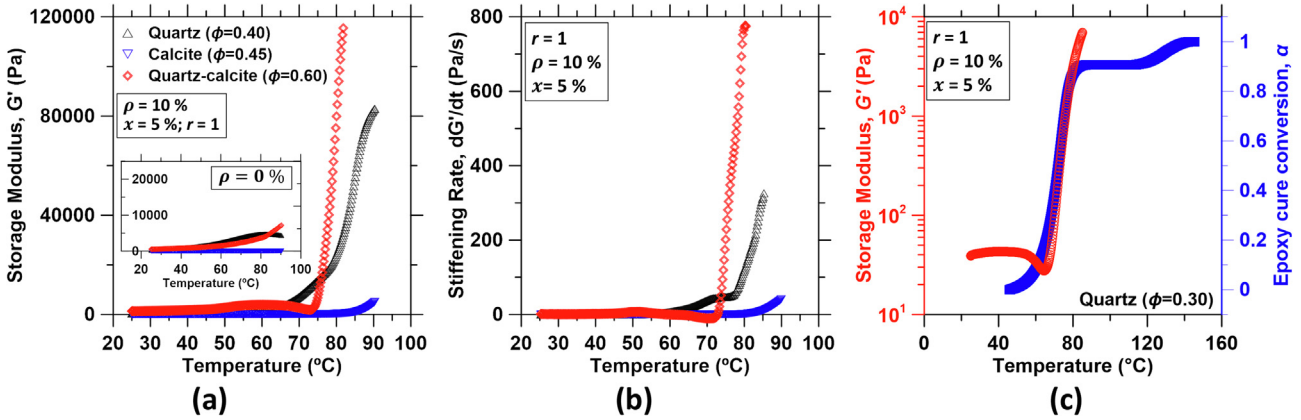


**Fig. 2.** **(a)** SAOS results illustrating the variation in elastic modulus $G'$ with temperature for different thermo-responsive suspensions across a range of solid loadings: quartz ($\phi = 0.40$), calcite ($\phi = 0.45$), 40/60 quartz-calcite mixture ($\phi = 0.60$). The inset shows the $G'$ variations with temperature for suspensions without resin. **(b)** Evolution of rate of change of $G'$ (i.e., $dG'/dt$) as a function of the temperature; **(c)** Illustration of the evolution of the elastic modulus and epoxy-thiol cure conversion in quartz suspension ($\phi = 0.30$) subjected to an identical heating rate. Note: for all data presented above, $G'$ evolutions were recorded during SAOS measurements with a temperature ramp of 2 °C/min. The epoxy-thiol conversion was estimated by integrating the DSC thermograms for a temperature ramp of 2 °C/min. For all the thermosensitive suspension formulations, resin dosage, $\rho$ = 10 % by mass of mineral particulates; initiator dosage, $x$ = 5 % by mass of resin, thiol-epoxy mass ratio, $r = 1$.

### 3.3. ***Optimizing thermoresponsiveness of mineral*** *suspensions*

Optimizing suspension formulations is necessary to reduce cost and augment the performance of thermosensitive materials. Here, near-inert quartz suspensions (i.e., very low dissolution rate) were chosen to illustrate and tailor thermoresponsive behavior and to elucidate the influence of solid volume fraction, resin content, initiator dosage, and the thiol-epoxy mixing ratio on the stiffening rate and mechanical strength of the cured composites. For instance, the thermally triggered stiffening of the mineral suspensions was affected by the solid volume fraction ($\phi$ = 0.30–0.45; see Fig. 3a and Figure S2a in the Supporting Information). $T_c$ reduced, and $G'$ increased at a faster rate upon activation of polymerization reactions with increasing $\phi$ (Fig. 3a). Similar behavior has been

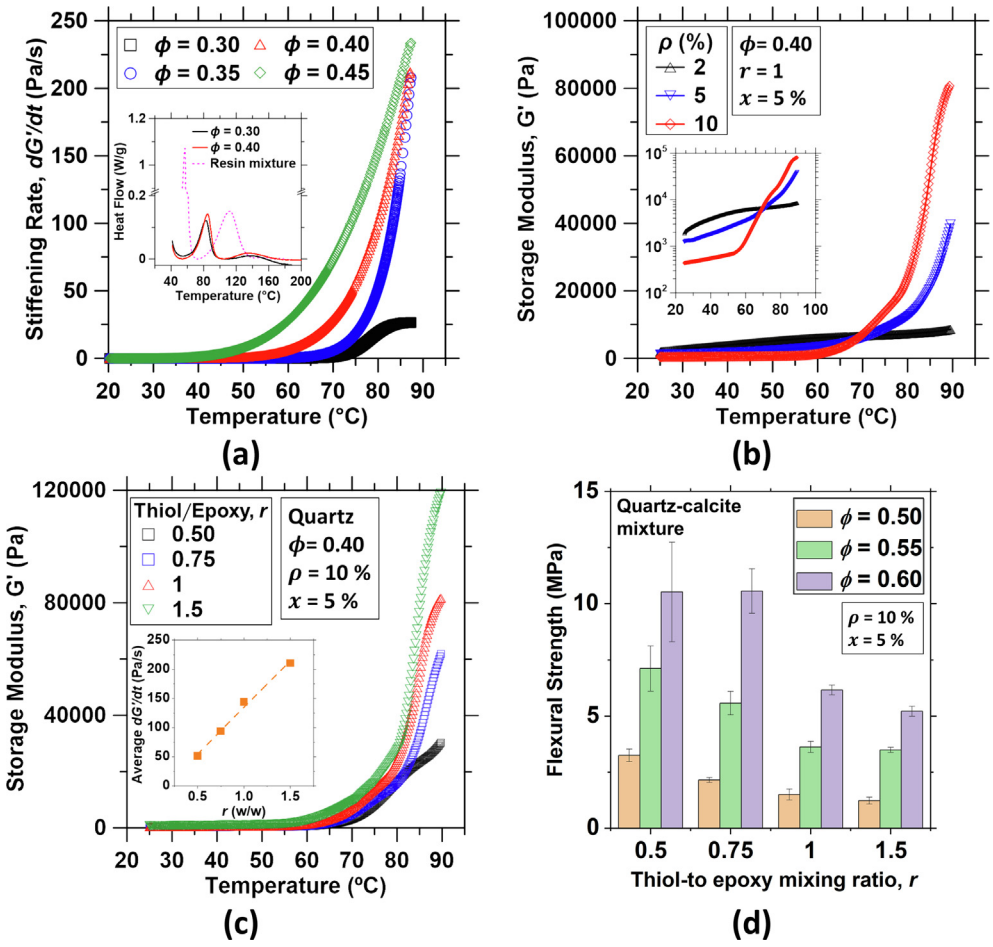


**Fig. 3.** **(a)** SAOS results showing the evolution of the rate of change of elastic modulus $G'$ (i.e. $dG'/dt$) with temperature for quartz suspensions for different $\phi$. The *inset* plot shows DSC thermograms at 5 °C/min for epoxy-resin mixture and quartz suspensions for different quartz contents (resin dosage, $\rho$=10 % by mass of quartz, initiator dosage, $x$ = 5 % by mass of resin, thiol-epoxy mass ratio, $r = 1$); **(b)** SAOS results illustrating the variation in $G'$ with temperature for quartz suspensions with different resin dosages $\rho$. The *inset* plot shows $G'$ evolution in log scale illustrating the reduction in low-temperature modulus with increasing $\rho$ (with $\phi = 0.40$, $r = 1$ and $x = 5$ %); **(c)** Variation in $G'$ of quartz suspensions as a function of temperature for formulations with different thiol-to-epoxy mixing ratios, $r$. The *inset* plot shows variations in the average stiffening rate (i.e., stiffening rate above $T_c$ is averaged) as a function of $r$(with $\phi = 0.40$, $\rho = 10$ % and $x = 5$ %); **(d)** An illustration of the variation in flexural strength of cured composites (for 40/60 quartz-calcite mixture suspensions with $\phi = 0.50$, 0.55 and 0.60, $\rho = 10$ % and $x = 5$ %) as a function of $r$.

previously reported for epoxy resin systems with silica fillers [52,60,61]. Insights into the physical underpinnings of these trends were sought by monitoring the curing kinetics of the epoxy-thiol resin mixtures and the epoxy-thiol-quartz suspensions with varying $\phi$. The exotherm height and area decreased while the peak exotherm temperature shifted to higher values for the epoxy-thiol-quartz suspensions as compared to the epoxy-thiol mixture (see *inset* of Fig. 3a). The decrease in the exotherm height and area is a consequence of the decreasing proportion of epoxy resin in the sample as the DSC heat flow signals are normalized with respect to the total mass of the sample. The broader epoxy-thiol curing exotherms of the suspensions as compared to a relatively sharper exotherm of the epoxy-thiol mixture suggest a slower cure reaction rate in suspensions. The retardation of the cure reaction and shift to higher temperatures in the mineral suspensions can be attributed to dilution effect (by the filler) and the increased viscosity of the formulation [52,62,63]. However, the total heat of epoxy-thiol cure reaction $\Delta h$ per epoxy equivalent showed no significant variation for both the systems (the average $\Delta h$ was found to be 104 kJ/eq ± 4 kJ/eq). Furthermore, no significant variation in peak exotherm temperature and the heat of reaction were observed upon increasing $\phi$ from 0.30 to 0.40. Thus, while the curing reaction is retarded in the mineral suspensions, the nearly constant heat of reaction suggests that the presence of the filler does not significantly influence the epoxy-thiol network structure formed. In addition, the decrease in $T_c$ with increasing $\phi$ cannot be ascribed to faster cure kinetics. Rather, the decrease in $T_c$ and the higher stiffening rate can rather be attributed to a decrease in the value of $\alpha$ required for the formation of a percolating network within the suspension. Because the particle aggregates are closer to each other in suspensions comprising higher $\phi$, the percolating network that restricts the particle-aggregate mobility and deformation forms at lower $\alpha$, resulting in a reduced $T_c$[26,52].

The thermoresponsive stiffening of the suspensions became increasingly evident as the resin loading in the suspension was increased (Fig. 3b). At the same time, the initial elastic modulus (i.e., low-temperature modulus) decreased as the resin content increased, suggesting an improved dispersion state of quartz particles [64]. The increase in resin content builds a denser crosslinked polymer network and binds the particle aggregates together, thereby enhancing thermo-stiffening. Thus, the resin dosage plays an essential role in controlling the low- and high-temperature fluidity and the thermoresponsiveness of these suspensions.

The thiol-to-epoxy mixing ratio affects the thermoresponsive stiffening as well as the mechanical strength of the cured hybrid composites (Fig. 3c and S2b). An increase in $r$ resulted in an

enhanced average stiffening rate (i.e., the average value of dG′/dt between $T_c$ and 90 °C, see *inset* of Fig. 3c), a modest decrease in the stiffening onset temperature, and a significant increase in the low temperature $G'$ (see Figure S2b). While the enhancement in the stiffening rate can be ascribed to the increasing contribution of the epoxy-thiol curing (i.e., the rapid and low-temperature curing that induces stiffening at temperatures below 90 °C) to the total epoxy curing, the enhancement in low temperature $G'$ suggests an aggregated particle state. A greater extent of aggregation is also expected to reduce the required cure conversion for the gelation, leading to a decrease in the stiffening onset temperature. We note that epoxy-thiol mixtures with $r < 0.5$ were reported to gel at the end of the first stage of curing [44]. Hence, formulations with $r < 0.5$ are not effective in inducing rapid thermosetting at temperatures below 90 °C. Overall, we observe that formulations with $r > 0.75$ crosslinked effectively during the first stage of curing, exhibiting rapid stiffening with an average stiffening rate > 100 Pa/s, which increases with increasing $r$ (Fig. 3c).

These trends in the thermostiffening response of the suspensions with varying $r$ were contrasted against the flexural strength and strain capacity of the cured composites to illustrate the effect on cured material properties due to the two-stage-polymer network formation. Formulations composed of a 40/60 mixture of quartz and calcite with $\phi$ = 0.50, 0.55, and 0.60 were chosen to evaluate the impact of $r$ on the flexural strength because: (1) their $\phi$ values are high enough to provide MPa level flexural strength while minimizing porosity and drying shrinkage, (2) the uncured suspensions exhibited sufficiently low viscosity at room temperature to ensure ease of flow through the extruder without clogging (e.g., for 3D printing applications), and (3) at $T > T_c$ suspensions exhibited rapid thermoresponsive stiffening.

The flexural strength of the cured composites increased with decreasing $r$ (Fig. 3d). For suspensions with $\phi = 0.60$, the cured composites exhibited a two-fold increase in flexural strength when $r$ was reduced from 1.5 (the stoichiometric formulation) to 0.5 (Fig. 3d). The higher strength with decreasing $r$ points to the formation of a tighter crosslinked polymer structure with an increasing fraction of epoxy homopolymer when formulated with excess epoxy ($r < 1.5$). Concomitantly, the failure strain of the cured composites reduced significantly with decreasing $r$ (Figure S3a). The decrease in $T_g$ of epoxy-thiol resin mixtures with increasing $r$ (Table 1) corroborates the increasing flexural strain capacity of the corresponding hybrid composites. The crosslinked polymer network, being central to the overall mechanical response of the hybrid composites, becomes rubbery and more flexible as $T_g$ drops below the ambient temperature with increasing $r$. Thus, an optimal $r$ for a thermosensitive formulation can be chosen to produce a targeted stiffening rate and final mechanical strength of the cured composite. Often, OPC-based suspensions exhibit a flexural strength typically between 3 and 10 MPa, depending on the water-to-cement ratio, chemical composition of cement, and degree of hydration [65–68]. Here, we limited our study to model mineral suspensions that are essentially non-reactive. Hence, the flexural strength primarily originates from the polymer binder and the friction between the mineral particles. Still, some of these composites (with $\phi = 0.60$ and $= 10\,\%$) exhibit flexural strength higher than 10 MPa. Evidently, flexural strength increases with the increase in resin content (Figure S3c).

At the same time, optimization of the initiator dosage ($x$) offers a route to modulate thermal latency and the induction period before the onset of thermostiffening response. An ideal nucleophilic initiator at an optimal dosage should offer a long induction period and asymptotically slow activation of the curing reaction at temperatures below the activation temperatures (i.e., $T < T_c$), and strong auto acceleration of the curing reaction when the suspension is heated above the activation temperature [36]. Increasing the dosage of the MI initiator resulted in a decrease in $T_c$ and an increased stiffening rate of the suspensions (Fig. 4a) while decreasing their low-temperature $G'$ (see *inset* of Fig. 4a). An initiator dosage of 5 % of MI helps to bring down $T_c$ below 60 °C and produces a sharp two orders of magnitude increase in $G'$ with an average stiffening rate of 144 Pa/s (red curve in Fig. 4a). The reduction in $T_c$ and the improved stiffening response at higher initiator concentrations can be attributed to the enhanced curing kinetics facilitated by the generation of a larger number of active species. Even though a higher $x$ results in a reduction in $T_c$, it can adversely affect the thermal latency and shorten the induction period. Quartz suspensions with $x = 5$ % exhibited a faster evolution of $G'$ at room temperature (i.e., 25 °C) than a suspension with $x = 2$ %, indicating initiation of the crosslinking reaction is promoted by the higher concentration of the initiator (Fig. 4b). Thus, high $x$ can accelerate epoxy-thiol cure kinetics leading to a shorter induction period and compromised thermal latency.

### 3.4. ***Design guidelines for thermoresponsive*** *suspensions*

The interplay of the critical parameters on the design of thermoresponsive suspensions for 3D printing of structural elements is illustrated in Fig. 5. For the current formulation, we recommend a range of $\phi$ and $\rho$ as a printable domain. The lower limit of $\phi$ is such that the cured suspensions provide at least 1 MPa flexural strength while minimizing porosity and drying shrinkage upon curing. The higher $\phi$ limit ensures that the suspensions' room temperature viscosity is sufficiently low to enable flow through the nozzle without jamming. Suspensions with their complex viscosity in the linear viscoelastic domain greater than the order of $10^4$ Pa.s are assumed to be non-extrudable since they could probably cause jamming in the pump and extruder. The recommended lower range of $\rho$ = 5 % is required to induce a noticeable thermoresponsive stiffening (Fig. 3b), and the maximum dosage is limited to 10% to limit the cost of printing slurries. Within the printable domain, the suspensions' stiffening rate (Fig. 3a-b) and cured composites' flexural strength (Fig. 3d and S3b-c) are directly proportional to their $\phi$ and $\rho$. Formulations with higher $\rho$ possess a denser crosslinked polymer network resulting in higher flexural strength (Figure S3b and S4). Similarly, a higher $\phi$ produces denser composites with lower porosity and higher flexural strength (Figure S3c). However, the extrudability (i.e., ease of flow) of the suspensions decreases with increasing $\phi$ and the material cost increases with increasing $\rho$. Coupling of these considerations with the influence of $r$ (Fig. 3c–d, S2b, and S3a) and $x$ (Fig. 4a–b) can enable the precise formulation of 3D printable mineral suspensions with thermally triggered curing that possess desired material properties, both pre-and post-extrusion.

### 3.5. ***Implementing 3D printing using thermoresponsive*** *slurries*

The thermoresponsive suspensions with controllable rapid solidification can enable 3D printing of structures that demand rapid hardening and high early strength. It can achieve higher overhangs, improved print height, print speed, and better print fidelity than conventional cementitious slurries. Controlled heating can be applied during extrusion and/or immediately after deposition. A single-stage heating at the nozzle or multi-stage heating with a preheating stage in the extruder to temperatures below $T_c$ can be utilized to heat the slurries during extrusion. Alternatively, a high-power heat gun can follow the print nozzle to heat the slurries just after deposition, potentially avoiding clogging of the print nozzle. However, implementing 3D printing using thermorespon-

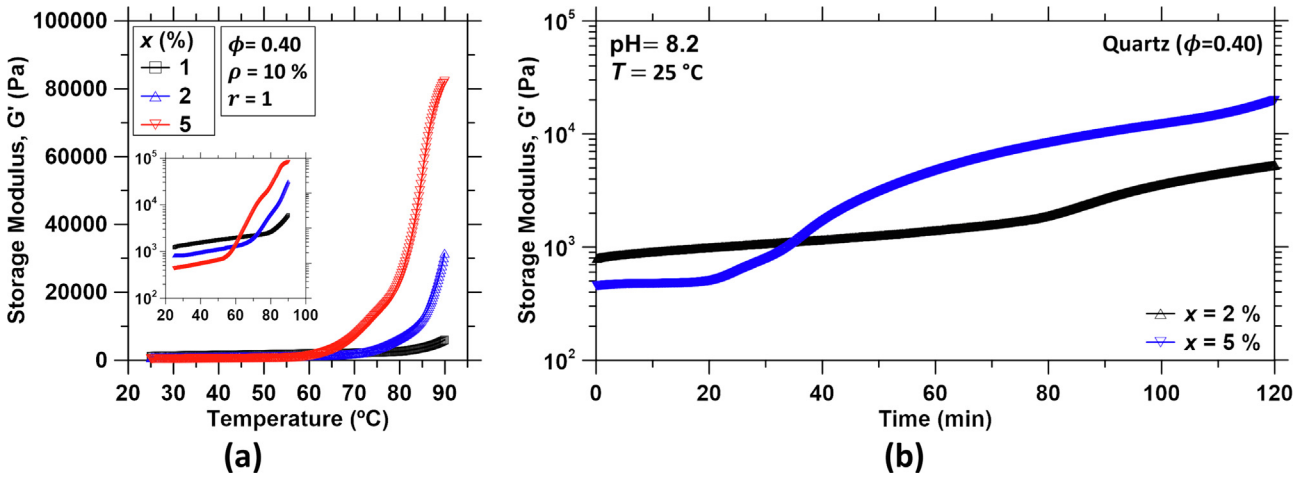


**Fig. 4.** **(a)** SAOS data illustrating the variation in elastic modulus $G'$ with temperature for different quartz formulations comprising different initiator dosages, $x = 1$ %, 2 %, and 5 % by mass of resin (with $\phi = 0.40$, $\rho = 10$ % by mass of quartz and $r = 1$). The inset shows $G'$ evolution in logarithmic scale illustrating the decreasing low-temperature $G'$ with increasing dosage of the initiator; **(b)** SAOS results depicting the variation in $G'$ at 25 °C with time for quartz thermo-responsive suspensions ($\phi = 0.40$) with different initiator dosages, $x = 2$ % and 5 % (with $r = 1$) to illustrate their thermal latency.

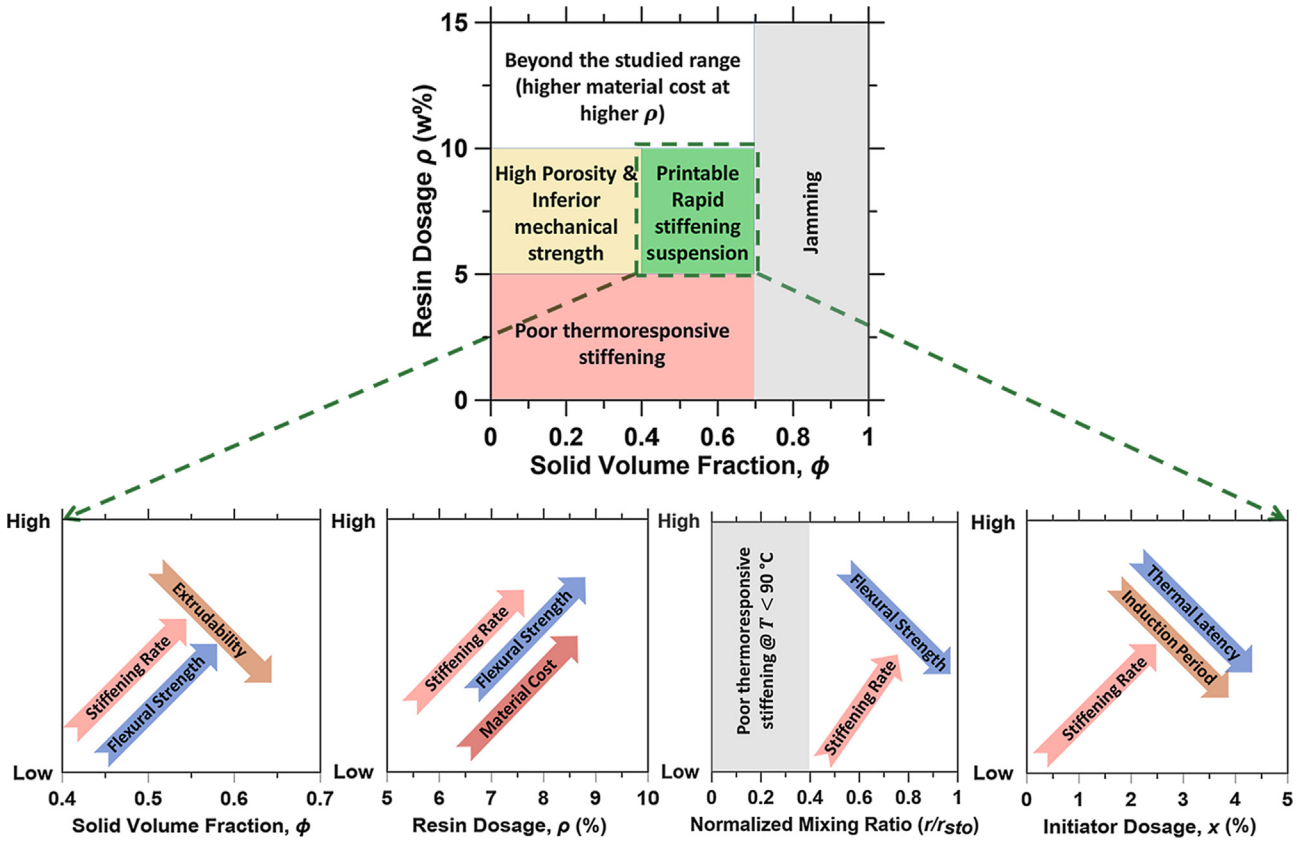


**Fig. 5.** A schematic of the interplay of the formulation parameters: solid volume fraction $\phi$, resin dosage $\rho$, thiol-to-epoxy mass ratio $r$, and initiator dosage $x$ on the performance of thermoresponsive suspensions for 3D-printing applications (Note: Here, the normalized mixing ratio is the ratio of thiol-to-epoxy mass ratio $r$ to the stochiometric thiol-to-epoxy mass ratio $r_{sto}$).

sive slurry will require a precise control and careful optimization of various process parameters, including heating rate, temperature, print speed, and nozzle diameter, to ensure printability and achieve the targeted slurry stiffness and stiffening rate. The geometrical complexity of the structure to be printed will dictate the target stiffness and rate of stiffening of the slurries. With specialized hardware capabilities, commensurate software controls, and dedicated (pre)processing methodology, thermoresponsive suspensions offer new pathways to overcome the limitations of traditional suspension-based printing and expand its scope to geometrically complex and topologically optimized structural components.

## 4. Summary and conclusions

The present study offers means for exploiting thermal triggers to formulate mineral suspensions that achieve desirable thermal latency and ultrafast stiffening – prerequisite attributes for 3D-manufacturing of architected structural components. Thermal latency, tunable induction period, and rapid stiffening are realized in concentrated suspensions by utilizing thermally triggered, 1-methylimidazole-catalyzed epoxy-thiol condensation-polymerization reactions of resins that are incorporated in the suspensions. The thermoresponsive suspensions comprise a thermosetting resin, a crosslinking agent reactive with the resin, water, and a large volume fraction of one or more mineral particulates. The formulations can be adjusted to achieve desirable thermal latency and stiffening rates. The thermoresponsive suspensions feature controllable ultrafast stiffening at trigger temperatures ranging between 50 °C and 90 °C, where the trigger temperature is sensitive to the initiator dosage. These suspensions undergo rapid solidification in a matter of seconds to minutes (activation time, $30 < t_a < 200$ s) upon bulk thermal activation achieving stiffening rates ranging from 20 Pa/s to 400 Pa/s. Curing of the suspensions at optimal conditions ensures the complete crosslinking of the thermoset resins that strengthens the composite. Epoxy excess in thiol–epoxy formulations and the resultant epoxy-homopolymerization produce a significant enhancement in the flexural strength of the mineral composites. The thermoresponsive suspensions, along with appropriate hardware capabilities, software controls, and dedicated processing methods, introduce formulation routes for extrusion-based 3D printing to produce overhangs, print highly stacked layers at a faster rate, and improve print fidelity.

In summary, we demonstrated a facile pathway to achieve controllable, rapid stiffening in aqueous suspensions that are compatible with extrusion-based additive manufacturing processes. This approach is economical and scalable for most construction materials, which are often opaque, have low electric conductivity, and possess a low surface-to-volume ratio. It is demonstrated that thermoresponsive formulations can be adjusted to produce controlled rapid stiffening at trigger temperatures ranging between 50 °C and 90 °C. Equally important, the current thermoresponsive formulations provide precise control over the engineered suspension compositions to achieve targeted, pre-and post-curing material properties. Taken together, the outcomes of this work offer a pathway to overcoming the limitations of suspension-based printing based on inorganic binders alone and expanding the design and production space accessible for architected structural components.

## Declaration of Competing Interest

The authors declare that they have no known competing financial interests or personal relationships that could have appeared to influence the work reported in this paper.

## Acknowledgments

The authors acknowledge the partial financial support for this research provided by the U.S. National Science Foundation (DMREF: 1922167), TRANSCEND, a joint UCLA-NIST Consortium that is funded by its industry and agency partners, Bavaria-California Technology Center (BaCaTec), The Advanced Research Projects Agency-Energy (ARPA-e: DE-AR-0001147), and the 3DConcrete Printing Network for Accelerating Progress in Concrete Additive Manufacturing supported by the U.S. National Science Foundation (AccelNet OISE: 2020095). This research was conducted in the Laboratory for the Chemistry of Construction Materials ($LC^2$) and the Electron Microscopy Core Facility at UCLA. The authors gratefully acknowledge the support provided by these laboratories that has made operations possible. The authors would also like to thank Gabriel Chemicals for providing GABEPRO GPM-800, and Dr. Shiying Zheng (Evonik Corporation) for many fruitful discussions. The contents of this paper reflect the views and opinions of the authors, who are responsible for the accuracy of the datasets presented herein, and do not reflect the views and/or policies of the funding agencies, nor do the contents constitute a specification, standard or regulation.

## Data Availability

The raw data required to reproduce these findings are available to download from [Raw Data]. The processed data required to reproduce these findings are available to download from [Processed Data].

## Appendix A. Supplementary material

Supplementary data to this article can be found online at https://doi.org/10.1016/j.matdes.2022.110905.

## References

[1] R.A. Buswell, W.R. Leal de Silva, S.Z. Jones, J. Dirrenberger, 3D printing using concrete extrusion: a roadmap for research, Cem. Concr. Res. 112 (2018) 37–49, https://doi.org/10.1016/j.cemconres.2018.05.006.
[2] C. Gosselin, R. Duballet, P. Roux, N. Gaudillière, J. Dirrenberger, P. Morel, Large-scale 3D printing of ultra-high performance concrete - a new processing route for architects and builders, Mater. Des. 100 (2016) 102–109, https://doi.org/10.1016/j.matdes.2016.03.097.
[3] V. Usmanov, D. Fakhri, M. Jogl, K. Kolář, SSP Modelling and manufacturing of complex architectural elements of concrete using industrial robots in formwork fabrication, Solid State Phenom. 309 (2020) 252–260, https://doi.org/10.4028/www.scientific.net/SSP.309.252.
[4] M.K. Mohan, A.V. Rahul, G. De Schutter, K. Van Tittelboom, Extrusion-based concrete 3D printing from a material perspective: a state-of-the-art review, Cem. Concr. Compos. 115 (2021), https://doi.org/10.1016/j.cemconcomp.2020.103855 103855.
[5] A. Anton, P. Bedarf, A. Yoo, B. Dillenburger, L. Reiter, T.F. Wangler, J. Robert, Concrete choreography: prefabrication of 3D-printed columns ETH Library, ETH Zürich Res, Collect. (2020).
[6] D. Lowke, E. Dini, A. Perrot, D. Weger, C. Gehlen, B. Dillenburger, Particle-bed 3D printing in concrete construction – possibilities and challenges, Cem. Concr. Res. 112 (2018) 50–65, https://doi.org/10.1016/j.cemconres.2018.05.018.
[7] G. De Schutter, K. Lesage, V. Mechtcherine, V.N. Nerella, G. Habert, I. Agusti-Juan, Vision of 3D printing with concrete — technical, economic and environmental potentials, Cem. Concr. Res. 112 (2018) 25–36, https://doi.org/10.1016/j.cemconres.2018.06.001.
[8] G. Kazakis, I. Kanellopoulos, S. Sotiropoulos, N.D. Lagaros, Topology optimization aided structural design: interpretation, computational aspects and 3D printing, Heliyon. 3 (2017), https://doi.org/10.1016/j.heliyon.2017.e00431 e00431.
[9] G. Vantyghem, W. De Corte, E. Shakour, O. Amir, 3D printing of a post-tensioned concrete girder designed by topology optimization, Autom. Constr. 112 (2020), https://doi.org/10.1016/j.autcon.2020.103084 103084.
[10] N. Roussel, Rheological requirements for printable concretes, Cem. Concr. Res. 112 (2018) 76–85, https://doi.org/10.1016/j.cemconres.2018.04.005.
[11] N. Roussel, H. Bessaies-Bey, S. Kawashima, D. Marchon, K. Vasilic, R. Wolfs, Recent advances on yield stress and elasticity of fresh cement-based materials, Cem. Concr. Res. 124 (2019), https://doi.org/10.1016/j.cemconres.2019.105798 105798.
[12] R.J.M. Wolfs, F.P. Bos, T.A.M. Salet, Early age mechanical behaviour of 3D printed concrete: numerical modelling and experimental testing, Cem. Concr. Res. 106 (2018) 103–116, https://doi.org/10.1016/j.cemconres.2018.02.001.
[13] B. García de Soto, I. Agustí-Juan, J. Hunhevicz, S. Joss, K. Graser, G. Habert, B.T. Adey, Productivity of digital fabrication in construction: cost and time analysis of a robotically built wall, Autom. Constr. 92 (2018) 297–311, https://doi.org/10.1016/j.autcon.2018.04.004.
[14] L. Reiter, T. Wangler, A. Anton, R.J. Flatt, Setting on demand for digital concrete: principles, measurements, chemistry and validation, Cem. Concr. Res. 132 (2020), https://doi.org/10.1016/j.cemconres.2020.106047 106047.
[15] A. M'Barki, L. Bocquet, A. Stevenson, Linking rheology and printability for dense and strong ceramics by direct ink writing, Sci. Rep. 7 (2017) 1–10, https://doi.org/10.1038/s41598-017-06115-0.

[16] A. Corker, H.C.H. Ng, R.J. Poole, E. García-Tuñón, 3D printing with 2D colloids: designing rheology protocols to predict "printability" of soft-materials, Soft Matter. 15 (2019) 1444–1456, https://doi.org/10.1039/c8sm01936c.
[17] V. Mechtcherine, F.P. Bos, A. Perrot, W.R.L. da Silva, V.N. Nerella, S. Fataei, R.J.M. Wolfs, M. Sonebi, N. Roussel, Extrusion-based additive manufacturing with cement-based materials – production steps, processes, and their underlying physics: a review, Cem. Concr. Res. 132 (2020), https://doi.org/10.1016/j.cemconres.2020.106037 106037.
[18] A. Perrot, D. Rangeard, A. Pierre, Structural built-up of cement-based materials used for 3D-printing extrusion techniques, Mater. Struct. 49 (2016) 1213–1220, https://doi.org/10.1617/s11527-015-0571-0.
[19] R.J.M. Wolfs, A.S.J. Suiker, Structural failure during extrusion-based 3D printing processes, Int. J. Adv. Manuf. Technol. 104 (2019) 565–584, https://doi.org/10.1007/s00170-019-03844-6.
[20] N. Roussel, G. Ovarlez, S. Garrault, C. Brumaud, The origins of thixotropy of fresh cement pastes, Cem. Concr. Res. 42 (2012) 148–157, https://doi.org/10.1016/j.cemconres.2011.09.004.
[21] N. Khalil, G. Aouad, K. El Cheikh, S. Rémond, Use of calcium sulfoaluminate cements for setting control of 3D-printing mortars, Constr. Build. Mater. 157 (2017) 382–391, https://doi.org/10.1016/j.conbuildmat.2017.09.109.
[22] N. Khalil, S. Rémond, B. Baz, G. Aouad, Characterization of 3D printing mortars made with OPC/CSA mixes, in: First RILEM Int. Conf. Concr. Digit. Fabr. – Digit. Concr. 2018, 2019: pp. 53–60. https://doi.org/10.1007/978-3-319-99519-9_5.
[23] L. Reiter, T. Wangler, N. Roussel, R.J. Flatt, The role of early age structural build-up in digital fabrication with concrete, Cem. Concr. Res. 112 (2018) 86–95, https://doi.org/10.1016/j.cemconres.2018.05.011.
[24] G. De Schutter, K. Lesage, Active control of properties of concrete: a (p)review, Mater. Struct. Constr. 51 (2018) 1–16, https://doi.org/10.1617/s11527-018-1256-2.
[25] J. Laarman, S. Jokic, P. Novikov, L.E. Fraguada, A. Markopoulou, Anti-gravity additive manufacturing, in: Fabr. 2014 Negot. Des. Mak., UCL Press, 2014: pp. 192–197.
[26] X. Wang, Y. Sun, C. Peng, H. Luo, R. Wang, D. Zhang, Transitional suspensions containing thermosensitive dispersant for three-dimensional printing, ACS Appl. Mater. Interfaces. 7 (2015) 26131–26136, https://doi.org/10.1021/acsami.5b07913.
[27] Y. Shangguan, M. Liu, L. Jin, M. Wang, Z. Wang, Q. Wu, Q. Zheng, Thermo-thickening behavior and its mechanism in a chitosan-graft-polyacrylamide aqueous solution, Soft Matter. 14 (2018) 6667–6677, https://doi.org/10.1039/c8sm00746b.
[28] N. Patil, A.C. Camacho, N.K. Mishra, P. Singhla, C.B. Sweeney, M.A. Saed, M. Radovic, M.J. Green, Radio frequency and microwave heating of preceramic polymer nanocomposites with applications in mold-free processing, Adv. Eng. Mater. 1900276 (2019) 1–8, https://doi.org/10.1002/adem.201900276.
[29] F. Scalera, C. Esposito Corcione, F. Montagna, A. Sannino, A. Maffezzoli, Development and characterization of UV curable epoxy/hydroxyapatite suspensions for stereolithography applied to bone tissue engineering, Ceram. Int. 40 (2014) 15455–15462, https://doi.org/10.1016/j.ceramint.2014.06.117.
[30] E. Zanchetta, M. Cattaldo, G. Franchin, M. Schwentenwein, J. Homa, G. Brusatin, P. Colombo, Stereolithography of SiOC ceramic microcomponents, Adv. Mater. 28 (2016) 370–376, https://doi.org/10.1002/adma.201503470.
[31] X. Mao, S. Shimai, M. Dong, S. Wang, Gelcasting of alumina using epoxy resin as a gelling agent, J. Am. Ceram. Soc. 90 (2007) 986–988, https://doi.org/10.1111/j.1551-2916.2007.01492.x.
[32] Y. Yang, W.M. Sigmund, A new approach to prepare highly loaded aqueous alumina suspensions with temperature sensitive rheological properties, J. Eur. Ceram. Soc. 23 (2003) 253–261, https://doi.org/10.1016/S0955-2219(02)00179-6.
[33] T. Chartier, C. Hinczewski, S. Corbel, UV curable systems for tape casting, J. Eur. Ceram. Soc. 19 (1999) 67–74, https://doi.org/10.1016/s0955-2219(98)00177-0.
[34] R.M. Loureiro, T.C. Amarelo, S.P. Abuin, E.R. Soulé, R.J.J. Williams, Kinetics of the epoxy-thiol click reaction initiated by a tertiary amine: calorimetric study using monofunctional components, Thermochim. Acta. 616 (2015) 79–86, https://doi.org/10.1016/j.tca.2015.08.012.
[35] M.C. Stuparu, A. Khan, Thiol-epoxy "click" chemistry: Application in preparation and postpolymerization modification of polymers, J. Polym. Sci. Part A Polym. Chem. 54 (2016) 3057–3070, https://doi.org/10.1002/pola.28195.
[36] A.O. Konuray, X. Fernández-Francos, X. Ramis, Analysis of the reaction mechanism of the thiol-epoxy addition initiated by nucleophilic tertiary amines, Polym. Chem. 8 (2017) 5934–5947, https://doi.org/10.1039/c7py01263b.
[37] B.D. Fairbanks, L.J. Macdougall, S. Mavila, J. Sinha, B.E. Kirkpatrick, K.S. Anseth, C.N. Bowman, Photoclick chemistry: a bright idea, Chem. Rev. 121 (2021) 6915–6990, https://doi.org/10.1021/acs.chemrev.0c01212.
[38] O. Konuray, X. Fernández-Francos, S. De la Flor, X. Ramis, À. Serra, The use of click-type reactions in the preparation of thermosets, Polymers. 12 (2020) 1084, https://doi.org/10.3390/POLYM12051084.
[39] K. Jin, W.H. Heath, J.M. Torkelson, Kinetics of multifunctional thiol-epoxy click reactions studied by differential scanning calorimetry: effects of catalysis and functionality, Polymer. 81 (2015) 70–78, https://doi.org/10.1016/j.polymer.2015.10.068.
[40] D. Guzmán, X. Ramis, X. Fernández-Francos, A. Serra, Enhancement in the glass transition temperature in latent thiol-epoxy click cured thermosets, Polymers. 7 (2015) 680–694, https://doi.org/10.3390/polym7040680.
[41] S. Vyazovkin, N. Sbirrazzuoli, Isoconversional kinetic analysis of thermally stimulated processes in polymers, Macromol. Rapid Commun. 27 (2006) 1515–1532, https://doi.org/10.1002/marc.200600404.
[42] S, Timoshenko, Strength of Materials, Part II - Advanced theory and problems, Huntington, NY, 1958 (reprint 1976), n.d.
[43] F.I. Baratta, G.D. Quinn, W.T. Matthews, Errors Associated with Flexure Testing of Brittle Materials (1987).
[44] X. Fernández-Francos, A.O. Konuray, A. Belmonte, S. De La Flor, À. Serra, X. Ramis, Sequential curing of off-stoichiometric thiol-epoxy thermosets with a custom-tailored structure, Polym. Chem. 7 (2016) 2280–2290, https://doi.org/10.1039/c6py00099a.
[45] X. Fernández-Francos, O. Konuray, X. Ramis, À. Serra, S. De la Flor, Enhancement of 3D-printable materials by dual-curing procedures, Materials. 14 (2021) 107, https://doi.org/10.3390/ma14010107.
[46] D. Guzmán, X. Ramis, X. Fernández-Francos, A. Serra, New catalysts for diglycidyl ether of bisphenol A curing based on thiol–epoxy click reaction, Eur. Polym. J. 59 (2014) 377–386, https://doi.org/10.1016/j.eurpolymj.2014.08.001.
[47] X. Fernández-Francos, D. Santiago, F. Ferrando, X. Ramis, J.M. Salla, À. Serra, M. Sangermano, Network structure and thermomechanical properties of hybrid DGEBA networks cured with 1-methylimidazole and hyperbranched poly (ethyleneimine)s, J. Polym. Sci. Part B Polym. Phys. 50 (2012) 1489–1503, https://doi.org/10.1002/polb.23145.
[48] C.E. Hoyle, A.B. Lowe, C.N. Bowman, Thiol-click chemistry: a multifaceted toolbox for small molecule and polymer synthesis, Chem. Soc. Rev. 39 (2010) 1355–1387, https://doi.org/10.1039/b901979k.
[49] J.A. Carioscia, J.W. Stansbury, C.N. Bowman, Evaluation and control of thiol-ene/thiol-epoxy hybrid networks, Polymer. 48 (2007) 1526–1532, https://doi.org/10.1016/j.polymer.2007.01.044.
[50] A.O. Konuray, X. Fernández-Francos, X. Ramis, Latent curing of epoxy-thiol thermosets, Polymer. 116 (2017) 191–203, https://doi.org/10.1016/j.polymer.2017.03.064.
[51] J.-P. Pascault, Thermosetting polymers, Marcel Dekker, New York, 2002.
[52] I. Isarn, L. Massagués, X. Ramis, À. Serra, F. Ferrando, New BN-epoxy composites obtained by thermal latent cationic curing with enhanced thermal conductivity, Compos. Part A Appl. Sci. Manuf. 103 (2017) 35–47, https://doi.org/10.1016/j.compositesa.2017.09.007.
[53] C.J. Rueb, C.F. Zukoski, Viscoelastic properties of colloidal gels, J. Rheol. (N. Y. N. Y). 41 (1997) 197–218, https://doi.org/10.1122/1.550812.
[54] S. Bhagavathi Kandy, I. Mehdipour, N. Neithalath, M. Bauchy, E. Garboczi, S. Srivastava, T. Gaedt, G. Sant, Temperature-induced aggregation in portlandite suspensions, Langmuir. 36 (2020) 10811–10821, https://doi.org/10.1021/acs.langmuir.0c01798.
[55] S. Moradi, Y. Calventus, F. Roman, J.M. Hutchinson, Achieving High Thermal Conductivity in Epoxy Composites : E ff ect of Boron Nitride Particle Size and Polymers. 11 (2019) 1156.
[56] I. Isarn, X. Ramis, F. Ferrando, A. Serra, Thermoconductive thermosetting composites based on boron nitride fillers and thiol-epoxy matrices, Polymers. 10 (2018) 277, https://doi.org/10.3390/polym10030277.
[57] P. Somasundaran, G.E. Agar, The zero point of charge of calcite, J. Colloid Interface Sci. 24 (1967) 433–440, https://doi.org/10.1016/0021-9797(67)90241-X.
[58] P.J. Flory, Principles of polymer chemistry, Cornell University Press, Ithaca, 1953.
[59] J.M. Hutchinson, S. Moradi, Thermal conductivity and cure kinetics of epoxy-boron nitride composites—a review, Materials. 13 (2020) 3634.
[60] H. Ng, I.C.A. Manas-zloczower, Filled epoxy resins, polym. Eng. Sci, Eng Sci. 33 (1993) 1–6.
[61] O. Becker, P. Sopade, R. Bourdonnay, P.J. Halley, G.P. Simon, Layered silicate nanocomposites based on various high-functionality epoxy resins. part II: the influence of an organoclay on the rheological behavior of epoxy prepolymers, Polym. Eng. Sci. 43 (2003) 1683–1690, https://doi.org/10.1002/pen.10142.
[62] I. Isarn, L. Bonnaud, L. Massagués, À. Serra, F. Ferrando, Study of the synergistic effect of boron nitride and carbon nanotubes in the improvement of thermal conductivity of epoxy composites, Polym. Int. 69 (2020) 280–290, https://doi.org/10.1002/pi.5949.
[63] J.M. Hutchinson, F. Román, A. Folch, Epoxy-thiol systems filled with boron nitride for high thermal conductivity applications, Polymers. 10 (2018), https://doi.org/10.3390/polym10030340.
[64] R.G. Larson, The structure and rheology of complex fluids, Oxford University Press, 1999.
[65] D.D. Higgins, J.E. Bailey, Fracture measurements on cement paste, J. Mater. Sci. 11 (1976) 1995–2003, https://doi.org/10.1007/bf02403347.
[66] B. Jd, H. Aj, K. k, Flexural strength and porosity of cements, Nature. 289 (1981) 388–390.
[67] M. Hambach, H. Möller, T. Neumann, D. Volkmer, Portland cement paste with aligned carbon fibers exhibiting exceptionally high flexural strength (> 100 MPa), Cem. Concr. Res. 89 (2016) 80–86, https://doi.org/10.1016/j.cemconres.2016.08.011.
[68] R. Liang, Q. Liu, D. Hou, Z. Li, G. Sun, Flexural strength enhancement of cement paste through monomer incorporation and in situ bond formation, Cem. Concr. Res. 152 (2022), https://doi.org/10.1016/j.cemconres.2021.106675 106675.